



Investigation of the wettability, anticorrosion, and accelerated weathering behaviors of siloxane-modified acrylic resin and functionalized graphene nanocomposite coatings on LY12 aluminum alloy

Paul C. Uzoma, Qiumeng Wang, Wanyu Zhang, Ning Jie Gao, Fuchun Liu, En-Hou Han

Received: 21 March 2020 / Revised: 5 November 2020 / Accepted: 13 November 2020
© American Coatings Association 2021

Abstract To expand the applications of graphene which has so far been limited by the expensive nature of single-layer graphene, the effects of varying percentages of low-cost functionalized multilayer graphene nanosheets in siloxane-modified organic coatings were studied. The hydrophobic organic siloxane–acrylic resin was prepared by solution polymerization of acrylic monomers, and the graphene nanosheets were functionalized using fluorosilane. The coatings were sprayed on the LY12 aluminum substrate, and the wettability, anticorrosion, conductive, and accelerated weathering behaviors were comprehensively examined. It is shown that the increasing

addition of functionalized graphene nanosheets increases the water contact angle and the surface conductivity. At 5% graphene loading, coating–substrate adhesion remains almost unchanged, while the electrochemical impedance parameters revealed good anticorrosion performance up to 10% loading. The surface measurements and Fourier transform infrared spectroscopy (FTIR) results confirmed the photostabilization ability of graphene loading in acrylic coatings during the accelerated weathering test. Also, the mechanical properties of the coatings were not damaged during the exposure, and pitting corrosion sites were observed only on the 20% graphene-filled coatings after 1000 h of exposure. These integrated analyses of mechanical properties and environmental accelerated tests are beneficial to engineering applications of graphene coatings.

Electronic supplementary material The online version of this article (<https://doi.org/10.1007/s11998-020-00443-z>) contains supplementary material, which is available to authorized users.

P. C. Uzoma, Q. Wang, W. Zhang, N. J. Gao, F. Liu (✉), E.-H. Han
Key Laboratory of Nuclear Materials and Safety Assessment, Institute of Metal Research, Chinese Academy of Sciences, Shenyang 110016, China
e-mail: feliu@imr.ac.cn

P. C. Uzoma, W. Zhang, N. J. Gao, F. Liu, E.-H. Han
School of Materials Science and Engineering, University of Science and Technology of China, Hefei 230026, China

P. C. Uzoma
Department of Polymer and Textile Engineering, Federal University of Technology, P.M.B. 1526, Owerri, Nigeria

F. Liu, E.-H. Han
Shenyang Zhongke Engineering Technology Center for Corrosion Control, Shenyang 110016, China

F. Liu, E.-H. Han
Institute of Corrosion Science and Technology, Guangzhou 510530, China

Keywords Nanocomposites, Graphene, Aluminum, Organic coatings, Superhydrophobic, Anticorrosion

Introduction

In contrast to bulk materials, nanoparticles and nanomaterials are known to possess a high surface to volume ratio which impacts several interesting functionalities on the subsequent behavior of these materials.¹ Therefore, nanomaterials have recently attracted extensive investigation as alternative materials for various engineering applications which include nanocomposite coatings.^{2–4} Nanocomposite coating is reportedly one of the fastest growing areas of nanotechnology research. These coatings are comprised of a host material with another material homogeneously embedded in it, having a characteristic length scale of nanometric range. They exhibit unique physical, mechanical, and functional properties and are also known to possess hardness values greater than that

obtained with the rule of a mixture.⁵ Before embedding into the host matrix, nanometer materials are often passed through surface modification processes.⁶ For the past few decades, nanoclay (e.g., montmorillonite), metallic nanoparticles, and carbon nanotubes are the most common nanofillers usually used in nanocomposite materials.^{7–12} However, the biodegradability and flexibility of montmorillonite can be compromised because it is a stiff inorganic platelet filler; hence, its application is limited.^{7,13} Also, metallic nanoparticles often pose a challenge of integration into the polymer matrices because they are not readily dispersed.^{7,14} Carbon nanotubes are seen as one of the most attractive promising nanofillers due to their high aspect ratio, low density, and outstanding mechanical properties.^{15–17} However, too much clustering resulting in poor dispersion, high cost, and low interfacial interactions with the polymeric matrices are among the most critical problems limiting the applications of carbon nanotubes in nanocomposite systems.⁷

Nowadays, graphene has occupied the center of research in nanocomposite materials since its discovery. Recent research has shown that it is more advantageous to use graphene; hence, it is more likely to be used as an alternative to carbon nanotubes in the polymer matrix, as it gives enhanced mechanical properties to the composite. This can be attributed to the planar structure and the aspect ratio provided during the loading process, which allows better stress distribution within the matrix. Also, researchers have revealed that the addition of a small fraction of the graphene component significantly improves the mechanical performance of the polymer matrix and impacts some extraordinary reinforcing and functional properties as well.^{7,15} Graphene is known to consist of a two-dimensional structure sheet with excellent properties¹⁸ which include a high specific surface area,¹⁹ high mechanical strength,²⁰ good conductivity,^{21,22} biocompatibility,²³ electrochemical and thermal properties.²⁴ These properties have made it a potential candidate material in various field applications such as nanocomposites, batteries, nanoelectronics, sensors, supercapacitors, biomedical, and hydrogen storage.²⁵

Several studies have examined the effect of graphene components on nanocomposite coatings which include monolayer graphene-coated copper by Ming et al.,²⁶ polystyrene/graphene-based nanocomposite by Yu et al.,²⁷ PMMA/graphene,²⁸ and epoxy/graphene.²⁹ Böhm suggested that the hydrophobic nature of pristine graphene makes it an excellent barrier to oxygen, water, and other corrosive agents. He also suggests that the electrical conductivity of graphene offers an alternative route to electrons generated at the anodic sites on the onset of corrosion, therefore, preventing them from reaching the cathodic sites resulting in an incomplete corrosion process.³⁰ Chang et al.³¹ confirmed the dispersion of graphene nanosheets in an epoxy matrix can reduce the oxygen diffusion pathway, thereby preventing the corrosion process. Raman et al.³² have proven that there is a

reduction in the corrosion rate of CVD-grown graphene on copper as a result of decreases in both anodic and cathodic current densities. Furthermore, studies have shown that graphene-based materials possess properties like anticorrosion, UV absorption, elasticity, and ultrahigh surface area which made them promising materials for antioxidant purposes.^{33–35} Mahdavian et al. treated graphene oxide with an ultraviolet absorber and added it into polyurethane (PU) coating before exposing it to an accelerated weathering test. Their studies showed that the treated graphene oxide coating offered three times more weathering stability when compared to blank PU coating.³⁶

Interestingly, one of the most important uses of acrylic polymers is in the area of surface coatings. This is largely due to their inherent optical clarity, good mechanical properties, chemical stability, and surface adhesion. They are also known to possess very high photostability, much higher than polyolefins.^{37,38} In this work, we varied the percentages of the functionalized low-cost seven-layer graphene nanosheets of 2.3 nm thickness in the silane-modified acrylic resin and evaluated their effects on the wettability and anticorrosion properties of the coatings. Furthermore, we analyzed the impact of the functionalized graphene on the accelerated weathering behaviors of the coatings.

Experimental

Materials

Siloxane–acrylic resin (synthesized in our laboratory),³⁹ and heptadecafluoro-1,1,2-tetradecyl triethoxysilane (fluorosilane) were purchased from Ark (Fogang) Chemical Material Co. Ltd., China. The graphene nanosheets were purchased from Ningbo Morsh Technology Co. Ltd., China. The graphene nanosheets were functionalized as reported by Uzoma et al.,³⁹ and the modification mechanism is represented in Fig. 1.

Coatings preparation

Before applying the coating, the LY12 substrates were polished with 600 grit sandpapers using a Unipol-820 Precision Metallographical Lapping/Polishing Machine to obtain an even rough surface, cleaned with distilled water and ethanol, and then dried under hot air. To obtain a nanopaste, the functionalized graphene nanosheet was dispersed in methyl isobutyl ketone (MIBK) for 30 min using a JY92-IIDN ultrasonic homogenizer. Various amount of the nanopaste was added into the organic siloxane–acrylic resin and stirred at the speed of 1000 rpm for 10 min. Thereafter, N3390 hardener was added to the mixture and stirred again for another 10 min. The air spray coating process

measurements were carried out to ensure data reproducibility.

The surface resistivities of the coatings were determined with an ACL 800 megohmmeter at 20°C and 26.3% relative humidity. The measurements are according to DIN EN 100 015/1 and ASTM D257 standards.

Accelerated weathering and physical property measurements

Accelerated weathering test was carried out using a QUV/spray accelerated weathering test chamber produced by Q-Lab Corporation USA. The chamber is equipped with UVA-340 fluorescent lamps (0.89 W m⁻² at 340 nm). The exposure cycles were kept at 8 h UV irradiation (60°C temperature) followed by 4 h condensation (50°C temperature). All the samples were exposed for 1000 h of combined irradiation and condensation cycles. Also, the gloss values were measured using BYK micro-gloss 60°.

Positest pull-off adhesion tester (Model AT-M) was employed to record the pull-off wet adhesion strength. An adhesive was used to attach the dollies perpendicular to the surface of the samples. The testing apparatus was attached to the dolly and positioned to apply tension perpendicular to the test surface; the force was steadily increased until the dolly was pulled off. The adhesion strength was taken to be the stress required to detach the dolly from the substrate. Average results were taken for each sample from multiple tests.

The crosscut dry adhesion test was carried out according to ASTM D 3002 and ASTM D 3359 standard, the impact test was done using SAC-GB/T 1732-93 standard.

Results and discussion

XPS survey of the functionalized graphene nanosheets

XPS technique was employed to characterize and identify the constituents' elements in the functionalized graphene nanosheets. Figure 2a shows that the XPS survey spectrum consists of Si 2p, C 1s, O 1s, and F 1s peaks which represent the elemental compositions present in the functionalized graphene. The atomic percentages of Si 2p, C 1s, O 1s, and F 1s from the survey scan are 1.23%, 76.76%, 3.72%, and 18.29%, respectively. Figures 2b-2e reveal the core-level spectrum of the functionalized graphene. The core-level Si 2p spectrum shows the binding energy peak at 103.1 eV which is attributed to SiO₂.⁴⁰ The core-level C 1s peaks were deconvoluted to effectively reveal the functionalities; the peak at 284.6 eV corresponds to the graphitic C-C, while the 291.8 eV peak is due to the CF₂-CF₂.^{41,42} The binding energy peak at 532.9 eV

shown by the core-level O 1s spectrum corresponds to the Si-O-Si bond which marks the characteristics of silane coupling.⁴³ Also, the core-level F 1s spectrum revealed binding energy of 689.2 eV, and this can be attributed to the CF₂-CF₂.⁴⁴ The presence of these functionalities at their respective signature peaks confirmed the successful functionalization of the graphene nanosheets.

Raman spectroscopy, TEM, and wettability analysis of the functionalized graphene nanosheets

The Raman spectra were recorded ranging from 500 to 3000 cm⁻¹ as shown in Fig. 3a. The D, G, and 2D bands for the unfunctionalized graphene nanosheets were obtained at 1333, 1586, and 2682 cm⁻¹, respectively, while for the functionalized graphene nanosheets, the D, G, and 2D bands were obtained at 1338, 1583, and 2682 cm⁻¹, respectively. The D bands indicate the breathing mode of sp³ carbon atoms, the G bands represent the phonon mode in-plane vibration of sp² carbon atoms, and 2D bands show the stacking order.⁴⁵ Also, the D/G intensity ratio (I_D/I_G) is used as an index to determine the graphene defects, and the 2D/G intensity ratio (I_{2D}/I_G) is used to qualify the number of stacked graphene layers. The I_D/I_G ratios of the unfunctionalized and functionalized graphene nanosheets are 0.47 and 0.17, respectively. Therefore, it shows that the structural defects on the graphene nanosheets were reduced during the modification process. The I_{2D}/I_G of both graphene samples is 0.03, proving that the graphene is a multilayer graphene structure because the I_{2D}/I_G ratios of < 1, 1-2, and 2-3 represent the multilayer, bilayer, and monolayer graphene, respectively.^{45,46}

Furthermore, the TEM image (Fig. 3b) revealed that the functionalized graphene nanosheets have spherical shapes with an average diameter of 33 nm. Figure 3c shows that the water droplets on the powders maintained their spherical shape and can easily roll on a slight tilt; the water contact angle on the modified powder is 151° which confirms the superhydrophobic property.

Surface wettability analysis

Acrylic resins have been reported to be hydrophilic with contact angles less than 90°^{47,48}; however, the synthesized resin is hydrophobic with a 94° water contact angle as a result of the presence of the low surface energy silane group. From the wettability measurement, we observed that increasing graphene nanosheet loading increases the water contact angles. The values obtained from G0 to G20 are 94°, 95.8°, 101.3°, 132°, and 152°, respectively. It can be seen that the increased presence of the superhydrophobic graphene in the coatings decreased the inherent surface polarity and the coatings' attraction to water.^{49,50} Figure S1 (supplementary mate-

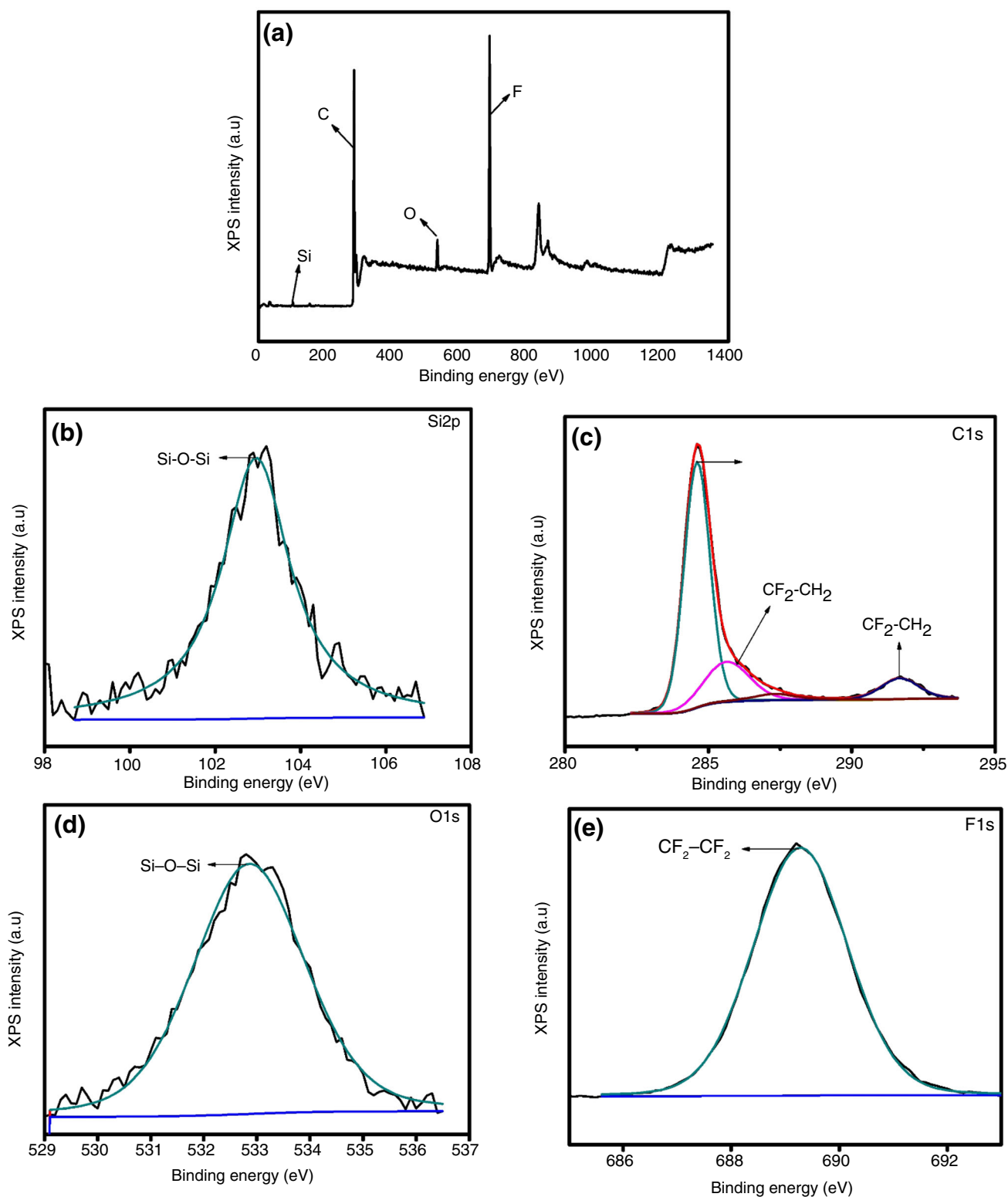


Fig. 2: XPS survey spectra of the modified graphene nanosheets: (a) wide-scan survey spectrum for all the elements. High-energy resolution spectra for (b) silica, (c) carbon, (d) oxygen, (e) fluorine signals

rials) shows the elemental compositions of the coating surface as dictated by energy-dispersive x-ray spectroscopy (EDX). G0 showed no presence of fluorine

element due to the absence of fluorosilane-functionalized graphene nanosheets; however, the presence of the fluorine element is observed in the other samples.

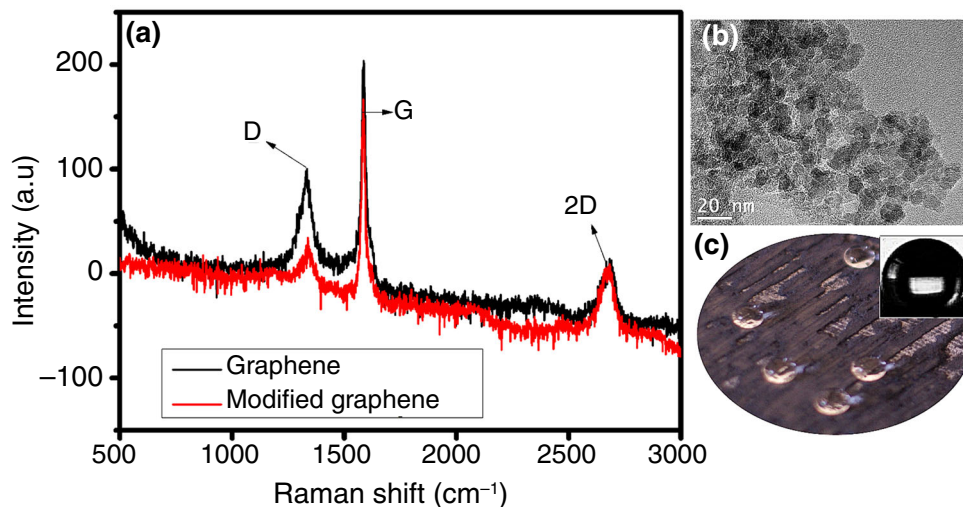


Fig. 3: (a) UV–Vis spectra; (b) TEM image of the modified graphene nanosheets. (The inserts are the images of the water droplets on the powder)

From the wettability results, we observed a rapid increase at G15 and also at G20 where the samples’ surface becomes superhydrophobic. The 10 μL water droplets stick to the surface of the hydrophobic coatings and will not slide when disturbed; however, on the superhydrophobic surface (G20), the water droplets have a sliding angle of 9° . The trapped air inside the textured surface of the superhydrophobic coating due to the nano-roughness factor is known to minimize the area of contact between the water droplet and the solid surface.^{50,51} There are noticeable increases in roughness on the samples surfaces from G0 to G20, as shown in the SEM and AFM images in Figs. 4 and 5, where R_a is the average roughness. Hence, from G15 to G20, there is a transition from the

Wenzel state to the Cassie–Baxter state. The Wenzel model is a complete wetting state where the water droplets are known to fully cover the microstructure of a textured surface; therefore, the surface exhibits relatively high adhesion.⁵² In the Cassie state, the water droplet is supported by the air pockets trapped inside textured surfaces to avoid droplet adhesion; the droplets only make contact with the peaks of the roughness elements.

EIS measurements

Electrochemical impedance spectroscopy (EIS) has been successfully used to examine corrosion protection

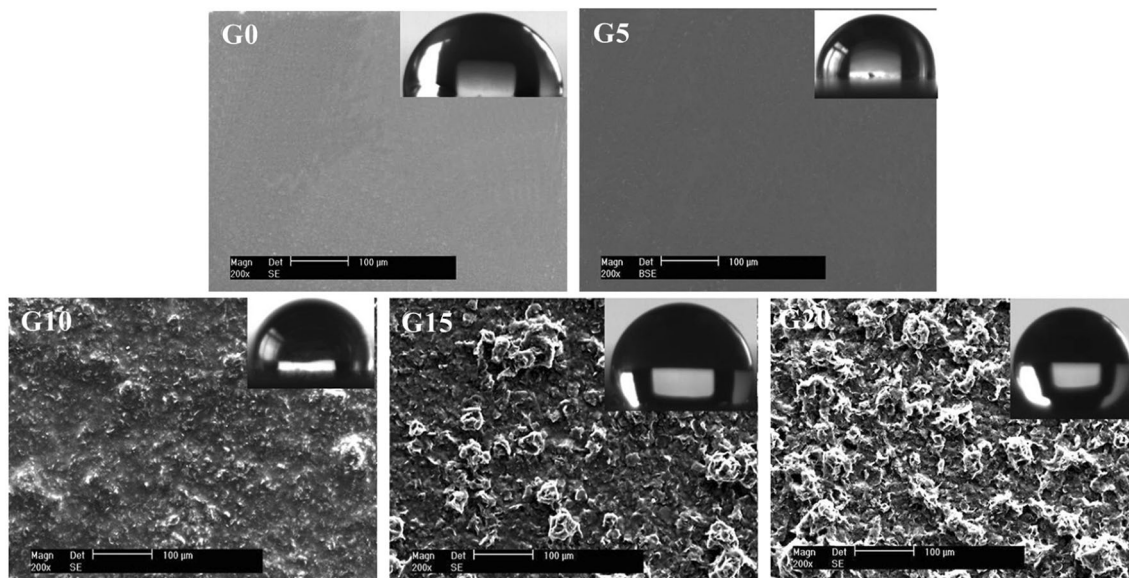


Fig. 4: SEM images of the coated samples (the inserts are the images of water droplets on the coatings)

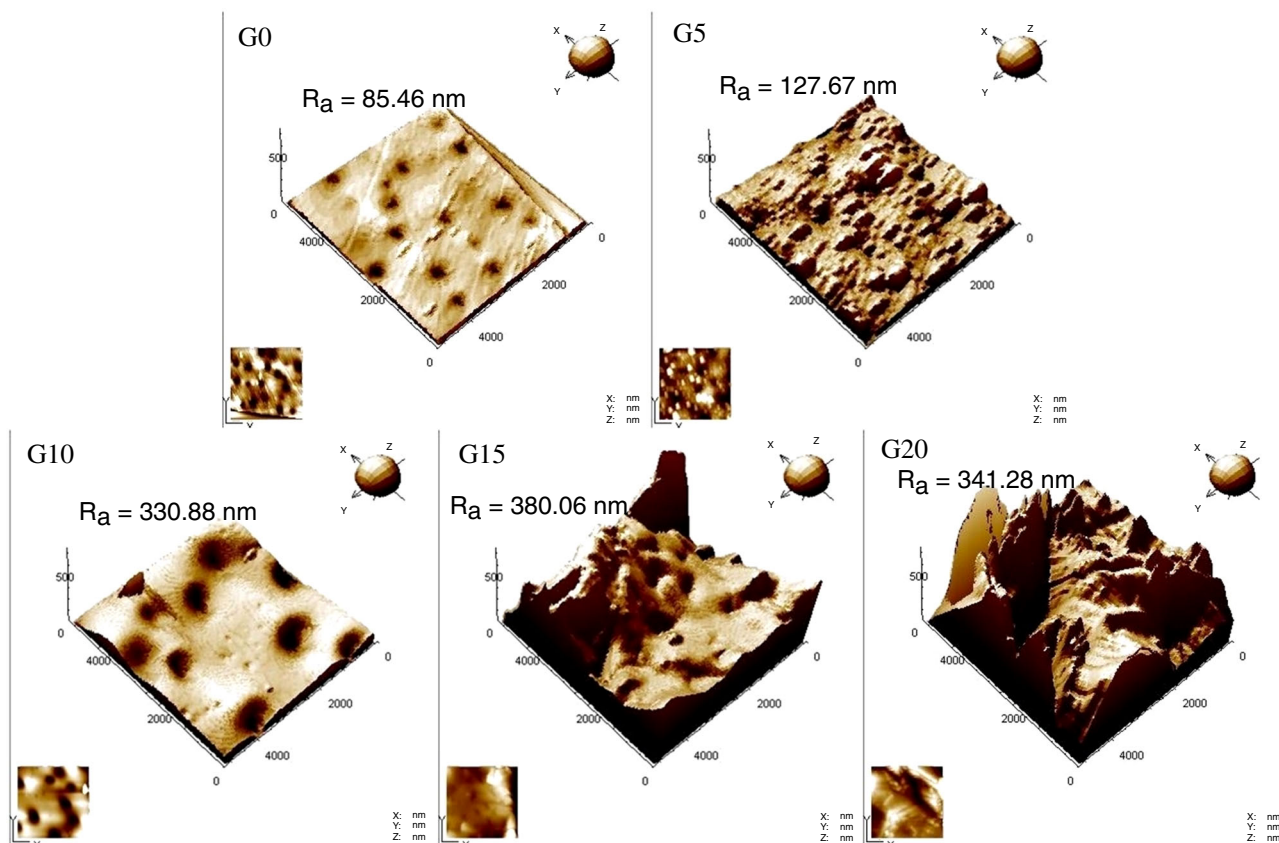


Fig. 5: AFM images revealing the surface roughness of the G0–G20 samples

of organic coatings because it gives a complete view of the coating degradation rate and the extent to which water and corrosive ions penetrate coatings.^{53–56} Therefore, EIS was employed to evaluate the anticorrosion capabilities of the coatings, and the data obtained were presented in Bode modulus and phase angle plots as a function of immersion time as shown in Figs. 6 and 7, respectively. Five equivalent electrical circuits (EECs) in Fig. 8 were used to appropriately analyze the various impedance data.

The electrical circuits in Fig. 8 include the electrolyte/solution resistance (R_s), constant phase elements (CPE) signifying the coating capacitance (Q_c), the coating resistance to the passage of electrolytes also known as the pores resistance (R_p), the constant phase elements representing the double layer capacitance between the metal surface/electrolyte solution (Q_{cdl}) and the charge transfer resistance across the metal surface (R_{ct}). Other additional components in the EEC include the Warburg finite diffusion impedance element (W), the inductance (L) which represents deposition of the passive layer, the diffusion capacitive component (Q_{diff}) and the diffusion resistance (R_{diff}), the salt film capacitance (Q_{sf}), and the salt film resistance (R_{sf}).

In the first 30 min of immersion, both the Bode modulus and phase angle plots of sample G0 in Figs. 6

and 7 exhibited a one-time constant capacitive loop; however, the equivalent electrical circuit in Fig. 8a approximately fits the plots when the dispersive number n is one ($n = 1$), indicating that Q_c exhibited purely capacitive behavior due to coating water absorption.⁵² The EEC used showed that partial electrochemical reaction has been initiated at the metal/coating interface but not largely pronounced at these systems, thereby causing overlapping of time relaxation of coating impedance and the impedance of the electrochemical reaction at the metal/coating interface.^{57,58} But as the immersion time increases, the time constants of impedance spectra begin to show three-time constants as revealed in the phase angle spectra which could be related to the large accumulation of corrosion products at the metal/coating interface. The initial high-frequency maximum at 10^3 – 10^5 Hz shows the capacitance of the coating, while the intermediate frequencies (10^{-1} – 10^2) are assigned to the capacitance of the aluminum oxide layer, and the corrosion process on the substrate is shown at the low-frequency time constant at 10^{-2} . The Bode modulus plot revealed a circular arc with a large radius; however, the radius decreased as the immersion time increased, signifying a reduced coating resistance and an increased capacitance due to water absorption. From 4 to 48 h of immersion, the EEC model in Figs. 8b and 8c exhibit-

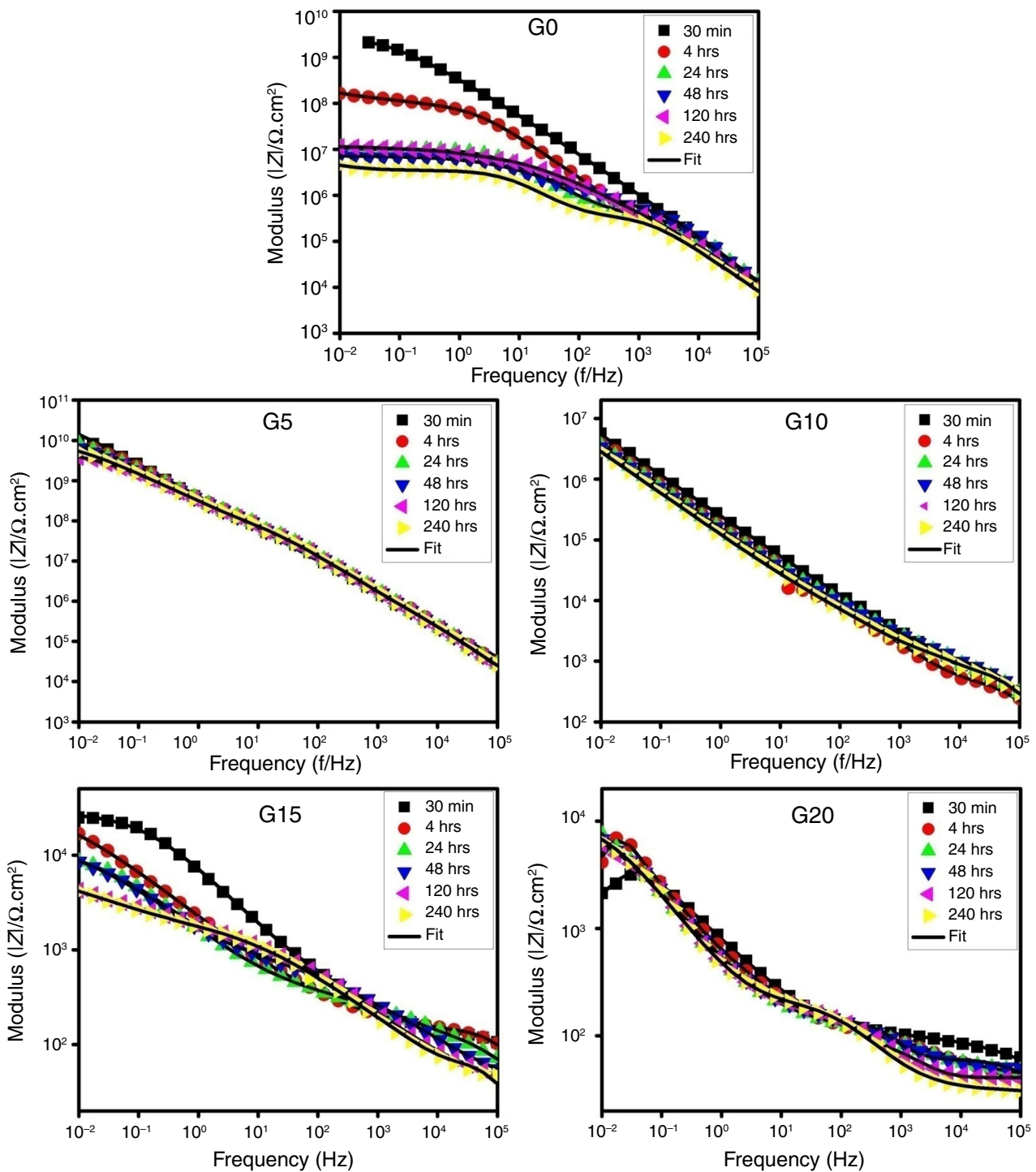


Fig. 6: Bode spectra showing the evolution of the impedance modulus against frequency with immersion time for the different coatings

ing three-time constants with Q_{diff} and R_{diff} components was adopted to fit the data. This takes into account the barrier performance against the diffusion of corrosion products from the metal surface toward the coating; in this case, the diffusion process may become the controlling factor in the Faradaic pro-

cesses. However, this diffusion behavior at both 4 and 24 h is not the ideal Warburg impedance since the value of n is not 0.5 (that is $n \neq 0.5$), whereas at 48 h the diffusion process behaves like an ideal Warburg impedance.⁵⁷

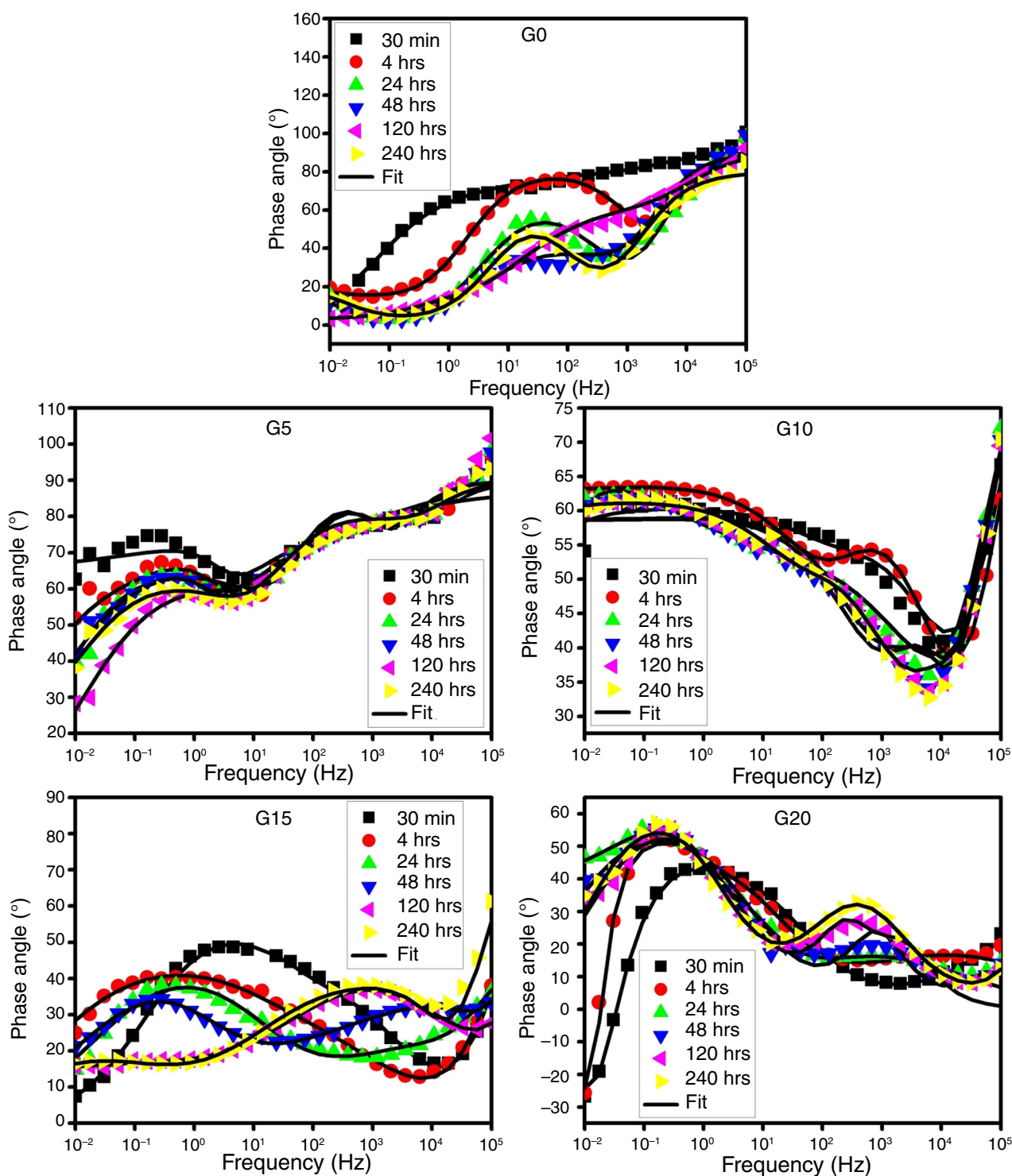


Fig. 7: Bode spectra showing the evolution of the phase angle against frequency with immersion time for the different coatings

There is always a deposition of salts film on the surface LY12 alloy whenever it is exposed to NaCl solution for a long period. This is as a result of the movement of Cl⁻ into the coatings/substrate interface.^{57,59} The G0 spectra from 120 to 240 h of immer-

sion showed four-time constants indicating the formation of corrosion products on the substrate; therefore, the EEC model in Fig. 8e is used to fit the 120-h and 240-h EIS spectra to account for the Q_{sf} and R_{sf} .

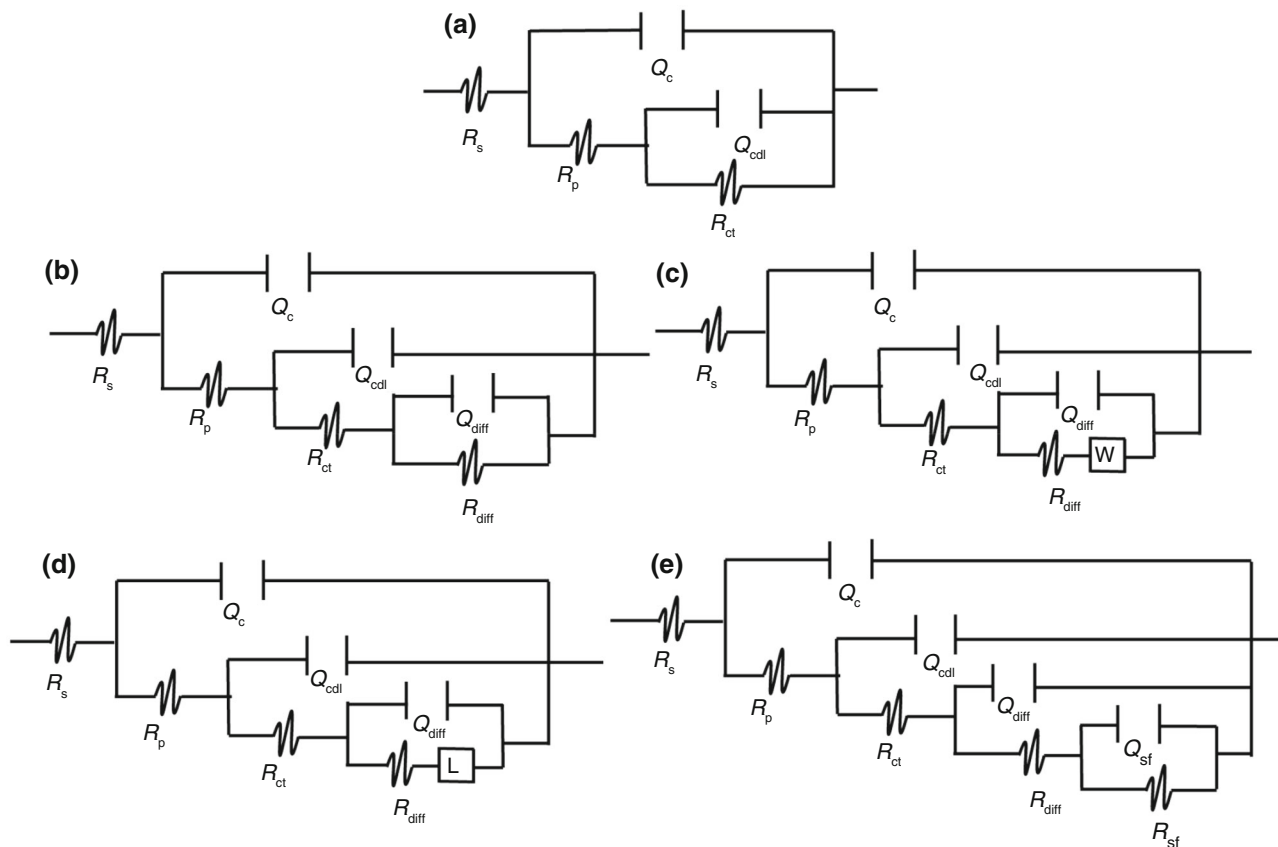


Fig. 8: Equivalent electric circuits: (a) two-time constants, (b) three-time constants, (c) three-time constants with diffusion element, *W*, (d) three-time constants with inductance element *L*, (e) four-time constants

There is an improvement in the corrosion performance at 5% graphene loading; however, at higher loads of graphene, the corrosion performance was significantly affected. Figure 7 shows that although there is an increase in the radius of the capacitive loop at 30 min immersion for G5, the radius decreased as the loading of graphene nanosheets increased. This can be attributed to among other things the less compact nature of the coatings as the graphene nanosheets loading increased which allowed aggressive electrolytes to penetrate the coating initiating the chemical reaction at the substrate/coating interface. The EEC model in Fig. 8a is adopted to fit the impedance spectra of G5 from 30 min to 120 h of immersion, while Fig. 8b approximately fits the spectra at 240 h of immersion, and also Fig. 8a–8e is adopted to fit the spectra of G10, G15, and G20 at different immersion times. For the superhydrophobic coating (G20), the phase angle plots in Fig. 7 show the presence of an inductive loop in the low-frequency range at the initial immersion time. Experimental reports have ascribed the low-frequency inductive loop to the layer stabilization by corrosion products of the corrosion reaction at the substrate/coating interface.⁶⁰ Besides, it is observed that the inductive loop disappeared as the time of immer-

sion increased, indicating that the corrosion reaction was reduced by the formation of oxide films.

Findings have shown that the impedance modulus obtained at low-frequency $|Z|_{0.01}$ is an appropriate measure for describing the corrosion protection of coatings, because the low-frequency range of the impedance explains the corrosion processes occurring at the substrate/coating interface, while the high-frequency range reveals information about the coatings.^{54,61} Hence, the impedance values at low-frequency $|Z|_{0.01}$ of our various coatings samples can be read from the Bode modulus plots in Fig. 6. It is shown that G0 has an impedance value of $2.11 \times 10^9 \Omega \text{ cm}^2$ at 30 min of immersion but steadily decreased to $4.54 \times 10^6 \Omega \text{ cm}^2$ after 240 h; this indicates the penetration of water and corrosive ions into the coating to the substrate/coating interface. G5 which is the highest performing coating has an initial value of $9.26 \times 10^9 \Omega \text{ cm}^2$, but it exhibited an insignificant decrease to $5.40 \times 10^9 \Omega \text{ cm}^2$ after 240 h of immersion. This proves that the coating G5 has good barrier protection to water and ion penetration, and can be attributed to the effect of the functionalized graphene present in the coating. The values of G10, G15, and G20 at 30 min of immersion are $5.60 \times 10^6 \Omega \text{ cm}^2$, $2.5 \times 10^4 \Omega \text{ cm}^2$, $2.14 \times 10^3 \Omega \text{ cm}^2$, respectively. However, after 240 h

of immersion, the values of G10 and G15 decreased to $2.85 \times 10^6 \Omega \text{ cm}^2$ and $4.15 \times 10^3 \Omega \text{ cm}^2$, respectively, while G20 experienced an increase to $6.43 \times 10^3 \Omega \text{ cm}^2$ after 240 h.

The charge transfer resistance (R_{ct}), the coating resistance (R_p), and the coating capacitance (C_c) as determined by the EIS fitting results were plotted as a function of immersion time, as shown in Fig. 9. The plots in Fig. 9a for R_{ct} showed a general trend of decrease in values after 240 h of immersion. Except for G10 that showed an initial increase before a gradual decrease with immersion time, other samples showed a sharp decrease in R_{ct} followed by a gradual decrease as immersion time increases. Furthermore, for R_p values (Fig. 9b), there is a general trend of negligible change in values as immersion time progresses, except for G5 which showed a sharp decrease initially and then followed by a gradual decrease. Previous studies have shown that there is the presence of pores and micro-holes in organic coatings which act as pathways for electrolyte diffusion.⁶² Therefore, this decrease in

values as observed in both R_{ct} and R_p can be ascribed to the presence of pores formation and degradation of the coatings as they interact with the corrosive electrolyte solution.⁵⁵ The gradual decrease later observed is a result of the formation of protective oxide which minimized the electrolyte penetration. Also, the higher R_p and R_{ct} values obtained in G0 and G5 indicate that the compactness of the coatings enhanced the protective barrier performance.⁶²

The coating capacitance C_c relates to water penetration into the coatings^{63,64}; in Fig. 9c, the plot of G0 showed an increase in the water uptake of the coatings. Researchers have proven that water penetration into coatings is a diffusion control process that includes the initial stage and the saturation stage. Interestingly, the introduction of the functionalized graphene into the coatings thereby deviating from the diffusion control process at the initial stage of immersion; this is shown by the decrease in water uptake as the time of immersion increased. This, therefore, dictates that the

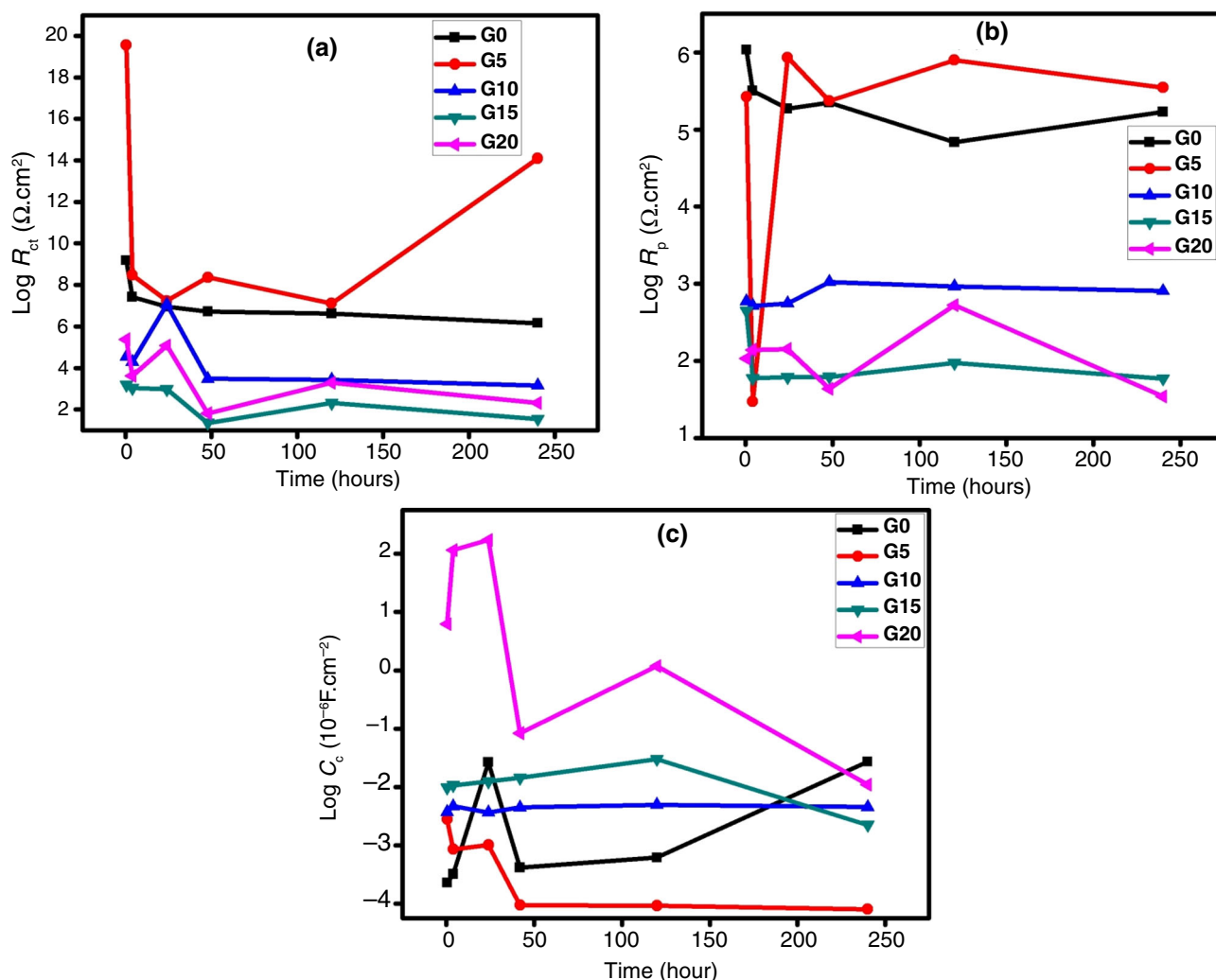


Fig. 9: Evolution of charge transfer resistance (a), pores resistance (b), and coatings capacitance (c) with immersion time

low energy materials present on the surface of the coatings minimized the surface affinity to water thereby reducing water penetration into the coatings.

Surface resistivity test

The surface resistivities of the coatings were measured, and the results obtained are $> 2 \times 10^{12} \Omega \text{ cm}^{-2}$, $7.88 \times 10^4 \Omega \text{ cm}^{-2}$, $1.45 \times 10^4 \Omega \text{ cm}^{-2}$, $1.48 \times 10^4 \Omega \text{ cm}^{-2}$, $< 10^3 \Omega \text{ cm}^{-2}$ for G0, G5, G10, G15, and G20, respectively. G0 sample is an insulating surface because of its high surface resistivity value which is greater than $10^{11} \Omega \text{ cm}^{-2}$ above which materials are considered to be insulators (ESD—electrostatic discharge association), and as the percentage graphene loading increases, the surface resistivity decreases, hence, increasing the conductivity of the coatings' surfaces. Other samples are categorized as conducting surfaces because their surface resistivity values are well below $10^6 \Omega \text{ cm}^{-2}$, below which materials are considered electrical conductors. From the literature, graphene has been successfully used to prepare conductive nanocomposites⁶⁵ and also used to improve electrical conductivities of organic coatings.^{66,67} To achieve a high electrical conductivity of composites, the distance between conducting particles should be reduced; hence, the increase in graphene contents increased the conductivity.⁶⁸

Wet adhesion strength

The wet adhesion strength is also known as the pull-off strength, and it is used to determine the greatest perpendicular force that a surface area of the coating can withstand before separating from the substrate. The results obtained reveal the compatibility of the coating's constituents and the substrate. The wet adhesion strength values for G0, G5, G10, G15, and G20 are 6.30, 6.05, 5.43, 4.51, and 3.85 MPa, respectively. The results show that at 5% loading, there is a negligible decrease in the adhesion strength; however, a significant decrease in the surface adhesion was observed at higher loadings. This is because, as various studies have shown, nanomaterials tend to cluster under high loading conditions due to high surface ratio, π - π bonding, and strong van der Waals forces. As a result, there is usually a failure to translate their excellent physical properties to the coating mixture, hence, the poor adhesion strength.⁶⁹ Also, by observing the dollies and the substrate, G0, G5, and G10 showed adhesive failure mode, whereas G15 and G20 revealed cohesive failure mode, as shown in Figure S2. In the coating composition as confirmed by the SEM results in Fig. 4, at lower percentage loading (5 wt% and 10 wt%), there is a complete envelope effect whereby the acrylic resin completely enclosed the graphene thereby making substrate adhesion resin dependent resulting in higher adhesion strength. However, as graphene load-

ing increased, the flaky shape features on the coated surfaces become increasingly significant thereby decreasing the resin's envelope effect. This shifts the substrate adhesion to graphene dependent, which results in lower adhesion strength. Furthermore, the presence of low surface energy material in the coatings reduced the coatings-substrate attraction resulting in low adhesion strength.

Accelerated weathering test

The influences of artificial sunlight (UV irradiation) and water condensation on the gloss, surface morphology, chemical structures, corrosion protection, wettability, and physical properties of the samples were examined via the accelerated weathering test. Gloss reduction is a common occurrence in the weathering of topcoats, and it can be a direct pointer to weathering degradation. This is because, at the onset of weathering degradation, polymeric chain scissions occur resulting in low molecular weight chains and water-soluble molecules. This gives rise to a certain degree of roughness on the coating's surface leading to light scattering and gloss reduction.³⁶ The initial gloss units for all the samples are 91.6, 14.5, 2.4, 0.6, and 0.5 for G0, G5, G10, G15, and G20, respectively. This indicates that the increasing addition of the functionalized graphene decreases the gloss units of the coating as a result of the black color of the graphene and the increase in the surface roughness. After 1000 h of accelerated weathering test, the gloss units become 76.9, 12.8, 1.1, 0.4, and 0.4 for G0, G5, G10, G15, and G20, respectively. The emphasis is on G0 and G5 since G10-G20 samples have near-zero gloss values. The decrease in the gloss unit of the G0 sample can be attributed to the increase in the surface roughness of the sample as observed in the AFM measurements in Fig. 10. As earlier discussed, it shows that there is the onset of weathering degradation process resulting in polymeric chain scissions in G0. For proper comparison, G0 and G5 samples with initial gloss units above 10 are considered. and, hence, improved stability of graphene-filled coatings when weathering tests are observed in G5 which revealed minimal reduction in gloss unit after 1000 h of exposure.

In addition, FTIR spectroscopy was used to accurately analyze the effect of the accelerated weathering on the chemical structures of the coatings. Generally, photooxidation of acrylic polymers often results in chain scission on the ester group with the formation of the gaseous product and extensive crosslinking reactions through macroradical recombination.³⁷ Figure 11 shows the difference in the normalized FTIR spectra of the various coatings before and after the accelerated weathering test. The spectra revealed the significant changes in the carbonyl (C=O) species frequencies in the range of 1600 – 1800 cm^{-1} and the hydroxyl (OH) groups in the range of 3200 – 3600 cm^{-1} . This is in agreement with the various literature that confirmed

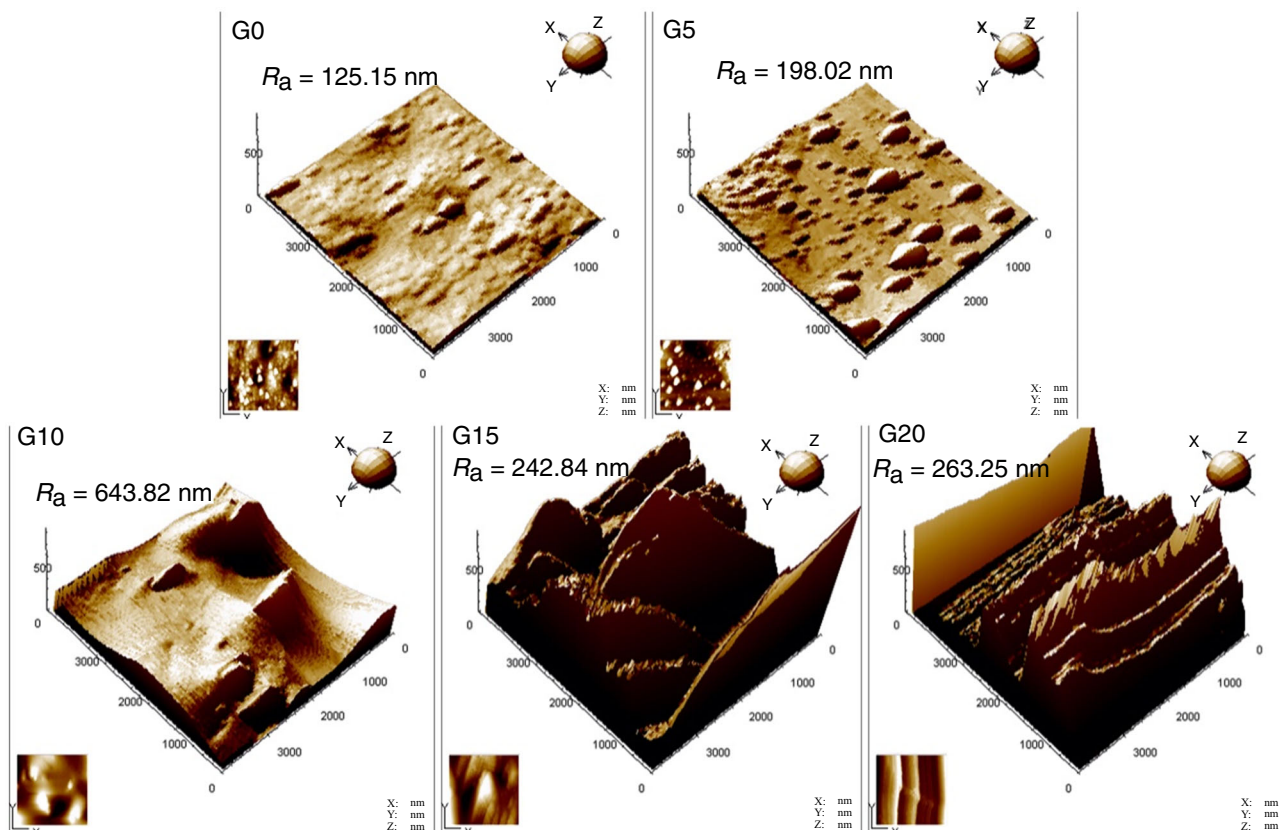


Fig. 10: AFM images revealing the surface roughness of the different samples after the accelerated weathering test

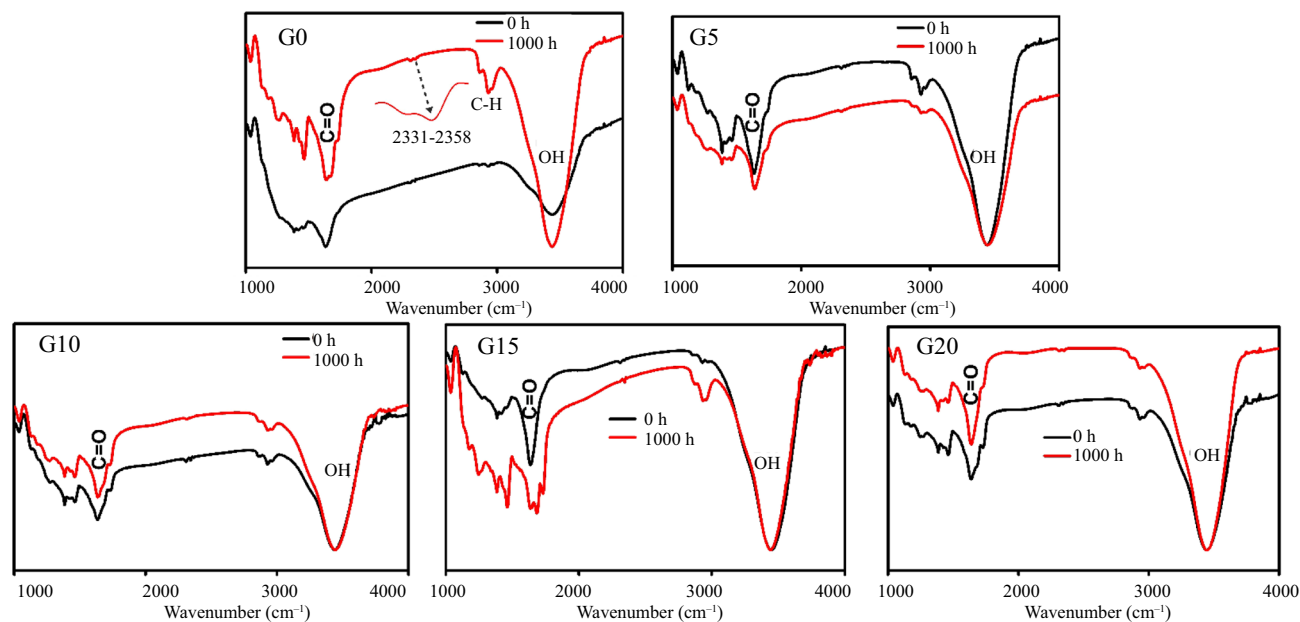


Fig. 11: Normalized FTIR spectra of all the coatings

that the main changes in UV irradiation of acrylic polymers are in the carbonyl species and hydroxyl groups.³⁷ When polyacrylates are irradiated in the presence of air, they produce radicals in the polymer

chains which react with oxygen to form new carbonyl compounds and hydroxyl groups.⁷⁰ The increase in the C=O bond is ascribed to the formation of γ -lactone structures which are known to absorb at 1780 cm^{-1} ,

and always occur in the photodegradation of all aliphatic polymers. It can also be attributed to the formation of acid groups due to photolysis of ketones. Furthermore, the broadened OH group is a result of the formation of carboxylic OH, alcohols, and peroxides.^{37,70} Besides, after the 1000 h of exposure, other bands appeared at 1303–1497 and 2823–3000 cm^{-1} particularly on the G0 and G5 plots. The increase in the band is attributed to the deformation of the symmetric and asymmetric aliphatic C–H groups. To better understand the changes in the chemical structure, the normalized values of the carbonyl and hydroxyl linkages are plotted in Fig. 12. The peak at 2331–2354 cm^{-1} was taken as the reference peak (a peak that has an identical intensity for all the coatings before and after the weathering test). The under-peak areas of the carbonyl and hydroxyl linkages were divided by the under-peak area of the reference peak.⁷¹ Figure 12 reveals a significant increase in the C=O and OH index of the G0 samples after 1000 h of the weathering test. It shows $\sim 255\%$ and $\sim 163\%$ increase in the C=O and OH groups, respectively. However, the graphene-filled coatings experience minimal changes when compared with the G0 samples. Interestingly, the G5 sample shows a reduction in the under-peak areas for both the C=O and OH groups. The decrease in OH value is probably due to the influence of the low surface energy material which inhibits water penetration into the coating. Therefore, fewer hydrolysis processes are shown to have occurred in the sample since water absorption is low. These findings indicate that there is inhibition of macroradical recombination in the graphene coatings, thus, impacting good photostabilization property. This is also in agreement with other research findings.³⁶

The SEM and the water contact angle images after the weathering tests are shown in Figure S2. The images reveal reduced roughness on the surfaces of G15 and G20 when compared to Fig. 4. Besides, sites of pitting corrosion are observed on the G15 and G20 surfaces, as shown in Figure S3. Also, a decrease in the

water contact angle was observed in all the samples after the exposure, the resultant water contact angle values are 60°, 70°, 95°, 109°, and 96° for G0, G5, G10, G15, and G20, respectively. The decrease in the water contact angle can be explained from a comparison of the SEM and AFM results before and after the weathering tests (Figs. 4, 5, 10, and S2). It suggests that the surface topographies of G15 and G20 are less developed after the weathering tests. This indicates that graphene protrusions which are initially present on the surfaces have been eroded, resulting in a significant decrease in the average roughness values after the weathering test. Also, the reduction in the water contact angle of G0–G10 samples can be attributed to the polymeric chain-breaking that results in the formation of water-soluble molecules, hence, increasing the coating's affinity for water.

Furthermore, to evaluate the effect of the graphene loading on the mechanical properties of the modified coatings before and after the accelerated weathering tests, the pull-off strength, crosscut dry adhesion, and impact tests were assessed. The pull-off strength values of the coatings after the weathering tests are 1.1, 2.1, 1.6, 1.4, and 1.1 MPa for G0–G20, respectively. Also, the G0, G5, and G10 showed adhesive failure mode, and G15 and G20 gave cohesive failure mode (Figure S5). The decrease in the pull-off strength for G0 can be attributed to the polymer chain degradation, as earlier discussed. Furthermore, the erosion of the surface roughness on the samples as seen in the AFM results could also lead to moisture migration into the coating–substrate interface thereby reducing the pull-off strength. The crosscut dry adhesion evaluates the resistance of the coatings to detaching from the substrate, while the impact test measures the ability of the coatings to resist cracking when struck with a load. The various pictures presented in Fig. 13 reveal that the dry adhesion integrity of the G0, G5, and G10 samples was not significantly affected by the addition of graphene nanosheets before and after the weathering test. The images show a minimal detachment of

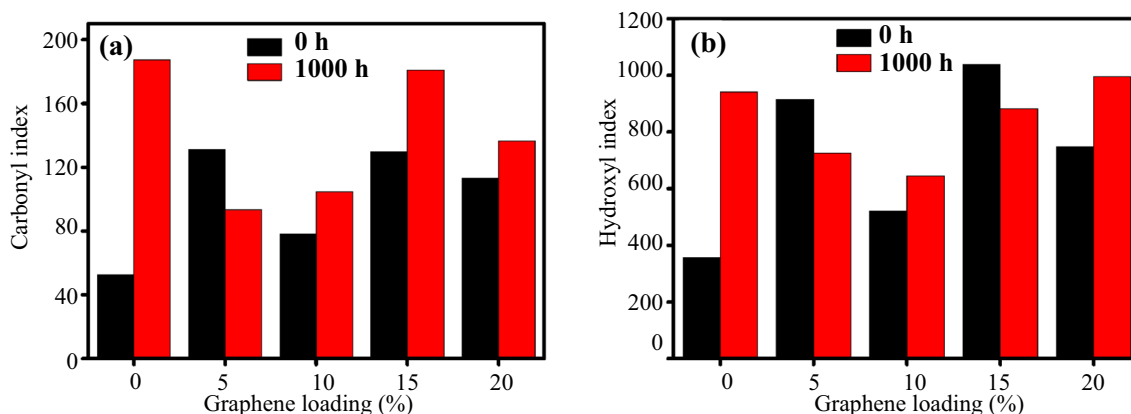


Fig. 12: (a) Carbonyl index, (b) hydroxyl index of the normalized FTIR plots of the coatings after the accelerated weathering test

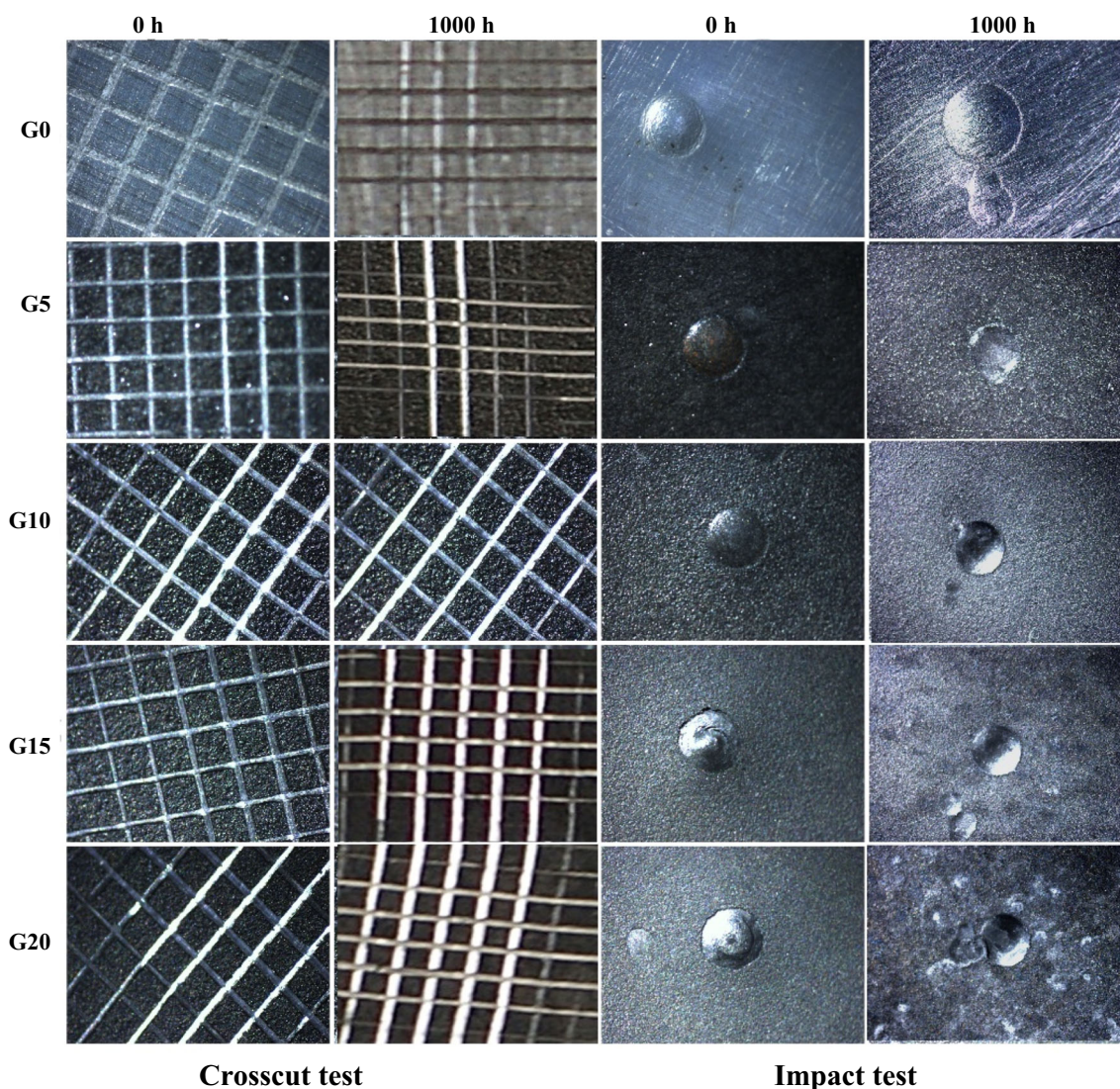


Fig. 13: Micrographic images of the crosscut and impact tests before and after QUV accelerated weathering test

small flakes at the intersection of the cuts maintaining the adhesion properties at ASTM class 4B for all the samples. However, the G15 and G20 samples decreased from class 4B to 3B indicating that flakes along the edges and the intersection of the cuts were detached. Besides, there is no impact failure from the images in Fig. 13 signifying that the coatings are not brittle.

Conclusion

The effects of varying percentages of fluorosilane-functionalized graphene nanosheets in siloxane–acrylic resin were investigated. The wettability results showed that an increase in the addition of the functionalized graphene increases the hydrophobic property such that at 20% loading, the coating was found to be superhydrophobic with a contact angle of 151.5° and a sliding

angle of 9° . The SEM and AFM results revealed a large increase in the surface roughness as the graphene loadings increased. The anticorrosion parameters proved that at lower loadings the coating can serve as a good corrosion protection barrier, and the EIS investigations revealed that 5% graphene loading gave the highest barrier performance and lowest degradation. Furthermore, the introduction of graphene into the coatings changes the surface resistivity from insulating to conducting surface. The wet adhesion strength remains unaffected at 5% loading; however, it decreases as the percentage graphene increases. The accelerated weathering test confirmed the stability of the functionalized graphene nanosheets when exposed to UV irradiation; it shows that the addition of graphene can block macroradical recombination and prevents the coating from photodegradation. Although there is a decrease in the pull-off strength after exposure, the mechanical integrities (crosscut adhesion

and impact strength) of the coatings were not significantly affected during the exposure. Furthermore, the corrosion protection barrier was preserved during the UV exposure for all the coatings except the 15% and 20% graphene-filled coatings. These integrated results provide a valuable contribution for graphene coatings in engineering applications.

Acknowledgments The authors acknowledge financial support from the Special Scientific Research on Civil Aircraft (MJ-2016-F-07), Guangzhou Industry-University Research Collaborative Innovation Alliance Special Subject (201604046014), and Shenyang Science and Technology Plan Project (Y17-1-039).

Conflict of interest The authors hereby declare that there is no conflict of interest regarding the publication of this article.

References

- Liu, F, Yang, L, Han, E, “Effect of Particle Sizes and Pigment Volume Concentrations on the Barrier Properties of Polyurethane Coatings.” *J. Coat. Technol. Res.*, **7** 301–313 (2010)
- Abu-Thabit, NY, Makhlof, ASH, “Recent Advances in Nanocomposite Coatings for Corrosion Protection Applications.” In: Makhlof, ASH, Scharnweber, D (eds.) *Handbook of Nanoceramic and Nanocomposite Coatings and Materials*, pp. 515–549. Butterworth-Heinemann, Oxford (2015)
- Liang, Y, Liu, F-C, Nie, M, Zhao, S, Lin, J, Han, E-H, “Influence of Nano-Al Concentrates on the Corrosion Resistance of Epoxy Coatings.” *J. Mater. Sci. Technol.*, **29** 353–358 (2013)
- Li, J, Yin, J, Ji, T, Feng, Y, Liu, Y, Zhao, H, Li, Y-P, Zhu, C-C, Yue, D, Su, B, Liu, X-X, “Microstructure Evolution Effect on High-Temperature Thermal Conductivity of LDPE/BNNS Investigated by In-situ SAXS.” *Mater. Lett.*, **234** 74–78 (2019)
- Santo, L, Davim, JP, “Nanocomposite Coatings: A review.” In: Paulo, DJ (ed.) *Materials and Surface Engineering*, pp. 97–120. Woodhead Publishing, Sawston (2012)
- Shi, H, Liu, F, Yang, L, Han, E, “Characterization of Protective Performance of Epoxy Reinforced with Nanometer-Sized TiO₂ and SiO₂.” *Prog. Org. Coat.*, **62** 359–368 (2008)
- Hu, K, Kulkarni, DD, Choi, I, Tsukruk, VV, “Graphene-Polymer Nanocomposites for Structural and Functional Applications.” *Prog. Polym. Sci.*, **39** 1934–1972 (2014)
- Wang, Z, Liu, F, Han, E, Ke, W, Luo, S, “Effect of ZnO Nanoparticles on Anti-aging Properties of Polyurethane Coating.” *Chin. Sci. Bull.*, **54** 3464 (2009)
- Wang, Z, Han, E, Liu, F, Ke, L, “Thermal Behavior of Nano-TiO₂ in Fire-Resistant Coating.” *J. Mater. Sci. Technol.*, **23** 547–550 (2007)
- Liu, X, Yin, J, Kong, Y, Chen, M, Feng, Y, Yan, K, Li, X, Su, B, Lei, Q, “Electrical and Mechanical Property Study on Three-Component Polyimide Nanocomposite Films with Titanium Dioxide and Montmorillonite.” *Thin Solid Films*, **544** 352–356 (2013)
- Liu, Y, Yin, J, Liu, X, Zhao, X, Chen, M, Li, J, Zhao, H, Zhu, C, Su, B, “Fabrication of Polymer Composite Films with Carbon Composite Nanofibers Doped MWNTs-OH for Multilevel Memory Device Application.” *Compos. Part B Eng.*, **156** 252–258 (2019)
- Huang, Y, Ouyang, QB, Zhang, D, Zhu, J, Li, RX, Yu, H, “Carbon Materials Reinforced Aluminum Composites: A Review.” *Acta Metall. Sin. (Engl. Lett.)*, **27** 775–786 (2014)
- Liu, F-C, Han, E-H, Ke, W, Tang, N, Wan, J, Yin, G, Deng, J, Zhao, K, “Polar Influence of the Organic Modifiers on the Structure of Montmorillonite in Epoxy Nanocomposites.” *J. Mater. Sci. Technol.*, **29** 1040–1046 (2013)
- Hou, Y, Cheng, YW, Hobson, T, Liu, J, “Design and Synthesis of Hierarchical MnO₂ Nanospheres/Carbon Nanotubes/Conducting Polymer Ternary Composite for High Performance Electrochemical Electrodes.” *Nano Lett.*, **10** 2727–2733 (2010)
- Sun, X, Sun, H, Li, H, Peng, H, “Developing Polymer Composite Materials: Carbon Nanotubes or Graphene?” *Adv. Mater.*, **25** 5153–5176 (2013)
- Li, X, Chen, BB, Jia, YH, Li, XF, Yang, J, Li, CS, Yan, FY, “Enhanced Tribological Properties of Epoxy-Based Lubricating Coatings Using Carbon Nanotubes-ZnS Hybrid.” *Surf. Coat. Technol.*, **344** 154–162 (2018)
- Ogawa, F, Yamamoto, S, Masuda, C, “Thermal Conductivity and Tensile Properties of Carbon Nanofiber-Reinforced Aluminum-Matrix Composites Fabricated via Powder Metallurgy: Effects of Ball Milling and Extrusion Conditions on Microstructures and Resultant Composite Properties.” *Acta Metall. Sin. (Engl. Lett.)*, **32** 573–584 (2019)
- Xu, J, Yi, DQ, Cui, Q, Wang, B, “Enhanced Wear Resistance of Ni/h-BN Composites with Graphene Addition Produced by Spark Plasma Sintering.” *Acta Metall. Sin. (Engl. Lett.)*, **32** 876–886 (2019)
- Wang, G, Shen, X, Wang, B, Yao, J, Park, J, “Synthesis and Characterisation of Hydrophilic and Organophilic Graphene Nanosheets.” *Carbon*, **47** (5) 1359–1364 (2009)
- Yoonessi, M, Gaier, JR, Peck, JA, Meado, MA, “Controlled Direction of Electrical and Mechanical Properties in Nickel Tethered Graphene Polyimide Nanocomposites Using Magnetic Field.” *Carbon*, **84** 375–382 (2015)
- Xiong, R, Hu, K, Grant, AM, Ma, R, Xu, W, Lu, C, Zhang, X, Tsukruk, VV, “Ultrarobust Transparent Cellulose Nanocrystal-Graphene Membranes with High Electrical Conductivity.” *Adv. Mater.*, **28** 1501–1509 (2016)
- Park, C-S, “Disorder Induced Transition of Electrical Properties of Graphene by Thermal Annealing.” *Results Phys.*, **9** 1534–1536 (2018)
- Qian, ZS, Shan, XY, Chai, LJ, Ma, JJ, Chen, JR, Feng, H, “A Universal Fluorescence Sensing Strategy Based on Biocompatible Graphene Quantum Dots and Graphene Oxide for the Detection of DNA.” *Nanoscale*, **6** (11) 5671–5674 (2014)
- An, S, Joshi, BN, Lee, J-G, Lee, MW, Kim, YI, Kim, M-W, Jo, HS, Yoon, SS, “A Comprehensive Review on Wettability, Desalination, and Purification Using Graphene-Based Materials at Water Interfaces.” *Catal. Today*, **295** 14–25 (2017)
- Mittal, G, Dhand, V, Rhee, KY, Park, S-J, Lee, WR, “A Review on Carbon Nanotubes and Graphene as Fillers in Reinforced Polymer Nanocomposites.” *J. Ind. Eng. Chem.*, **21** 11–25 (2015)
- Ming, HL, Wang, SY, Zhang, ZM, Wang, JQ, Han, EH, Ke, W, “Oxidation and Electrochemical Behavior of Monolayer-

- Graphene-Coated Copper in Simulated Primary Water.” *Acta Metall. Sin. (Engl. Lett.)*, **29** 89–93 (2016)
27. Yu, Y-H, Lin, Y-Y, Lin, C-H, Chan, C-C, Huang, Y-C, “High-Performance Polystyrene/Graphene-Based Nanocomposites with Excellent Anti-corrosion Properties.” *Polym. Chem.*, **5** 535–550 (2015)
 28. Chang, K-C, Ji, W-F, Lai, M-C, Hsiao, Y-R, Hsu, C-H, Chuang, T-L, Wei, Y, Yeh, J-M, Liu, W-R, “Synergistic Effects of Hydrophobicity and Gas Barrier Properties on the Anticorrosion Property of PMMA Nanocomposite Coatings Embedded with Graphene Nanosheets.” *Polym. Chem.*, **5** 1049–1056 (2014)
 29. Monetta, T, Acquesta, A, Carangelo, A, Bellucci, F, “The Effect of Graphene Loading on the Corrosion Resistance of Organic Coatings.” *Metall. Ital.*, **7** 91–94 (2017)
 30. Böhm, S, “Graphene Against Corrosion.” *Nature Nanotechnology*, **9** 741–742 (2014)
 31. Chang, K-C, Hsu, M-H, Lu, H-I, Lai, M-C, Liu, P-J, Hsu, C-H, Ji, W-F, Chuang, T-L, Wei, Y, Yeh, J-M, Liu, W-R, “Room-Temperature Cured Hydrophobic Epoxy/Graphene Composites as Corrosion Inhibitor for Cold-Rolled Steel.” *Carbon*, **66** 144–153 (2014)
 32. Raman, RKS, Banerjee, P-C, Lobo, D-E, Gullapalli, H, Sumandasa, M, Kumar, A, Choudhary, L, Tkacz, R, Ajayan, P-M, Majumder, M, “Protecting Copper from Electrochemical Degradation by Graphene Coating.” *Carbon*, **50** 4040–4045 (2012)
 33. Qiu, Y, Wang, Z, Owens, A-C, Kulaots, I, Chen, Y, Kane, A-B, Hurt, R-H, “Antioxidant Chemistry of Graphene-Based Materials and Its Role in Oxidation Protection Technology.” *Nanoscale*, **6** 11744–11755 (2014)
 34. Dutta, D, Ganda, A-N-F, Chih, J-K, Huang, C-C, Tseng, C-J, Su, C-Y, “Revisiting Graphene-Polymer Nanocomposite for Enhancing Anticorrosion Performance: A New Insight into Interface Chemistry and Diffusion Model.” *Nanoscale*, **10** (26) 12612–12624 (2018)
 35. Chang, K-C, Ji, W-F, Lai, M-C, Hsiao, Y-R, Hsu, C-H, Chuang, T-L, Wei, Y, Yeh, J-M, Liu, W-R, “Synergistic Effects of Hydrophobicity and Gas Barrier Properties on the Anticorrosion Property of PMMA Nanocomposite Coatings Embedded with Graphene Nanosheets.” *Polymer Chemistry*, **5** (3) 1049–1056 (2014)
 36. Mahdavian, M, Yari, H, Ramezanzadeh, B, Bahlakeh, G, Hasani, M, “Immobilization of Ultraviolet Absorbers on Graphene Oxide Nanosheets to be Utilized as a Multifunctional Hybrid UV-Blocker: A Combined Density Functional Theory and Practical Application.” *Appl. Surf. Sci.*, **447** 135–151 (2018)
 37. Chiantore, O, Trossarelli, L, Lazzari, M, “Photooxidative Degradation of Acrylic and Methacrylic Polymers.” *Polym. Chem.*, **41** 1657–1668 (2000)
 38. Aguirre, M, Goikoetxea, M, Otero, L-A, Paulis, M, Leiza, J-R, “Accelerated Ageing of Hybrid Acrylic Waterborne Coatings Containing Metal Oxide Nanoparticles: Effect on the Microstructure.” *Surf. Coat. Technol.*, **321** 484–490 (2017)
 39. Uzoma, P-C, Liu, F, Xu, L, Zhang, Z, Han, E-H, Ke, W, Arukalam, I-O, “Superhydrophobicity, Conductivity and Anticorrosion of Robust Siloxane-Acrylic Coatings Modified with Graphene Nanosheets.” *Prog. Org. Coat.*, **127** 239–251 (2019)
 40. Alam, A-U, Howlader, M-M-R, Deen, M-J, “Oxygen Plasma and Humidity Dependent Surface Analysis of Silicon, Silicon Dioxide and Glass for Direct Wafer Bonding.” *ECS J. Solid State Sc. Technol.*, **2** (12) 515–523 (2013)
 41. Zhang, X, Ma, Y, Zhao, C, Yang, W, “High Dielectric Constant and Low Dielectric Loss Hybrid Nanocomposites Fabricated with Ferroelectric Polymer Matrix and BaTiO₃ Nanofibers Modified with Perfluoroalkylsilane.” *Appl. Surf. Sci.*, **305** 531–538 (2014)
 42. Uzoma, P-C, Liu, F, Han, E-H, “Multi-stimuli-Triggered and Self-Repairable Fluorocarbon Organic Coatings with Urea-Formaldehyde Microcapsules Filled with Fluorosilane.” *J. Mater. Sci. Technol.*, **45** 70–83 (2020)
 43. Liang, J, Wu, X-W, Ling, Y, Yu, S, Zhang, Z, “Trilaminar Structure Hydrophobic Graphene Oxide Decorated Organosilane Composite Coatings for Corrosion Protection.” *Surf. Coat. Technol.*, **339** 65–77 (2018)
 44. Puniredd, S-R, Assad, O, Haick, H, “Highly Stable Organic Monolayers for Reacting Silicon with Further Functionalities: The Effect of the C–C Bond Nearest the Silicon Surface.” *J. Am. Chem. Soc.*, **130** 13727–13734 (2008)
 45. Teng, T-P, Chang, S-C, Chen, Z-Y, Huang, C-K, Tseng, S-F, Yang, C-R, “High-Yield Production of Graphene Flakes Using a Novel Electrochemical/Mechanical Hybrid Exfoliation.” *Int. J. Adv. Manuf. Technol.*, **104** (5) 2751–2760 (2019)
 46. Nguyen, V-T, Le, H-D, Nguyen, V-C, Ngo, T-T, Le, D-Q, Nguyen, X-N, et al., “Synthesis of Multi-layer Graphene Films on Copper Tape by Atmospheric Pressure Chemical Vapor Deposition Method.” *Advances in Natural Sciences: Nanoscience and Nanotechnology*, **4** (3) 035012 (2013)
 47. Sabatini, V, Cattò, C, Cappelletti, G, Cappitelli, F, Antenucci, S, Farina, H, Ortenzi, M-A, Camazzola, S, Di Silvestro, G, “Protective Features, Durability and Biodegradation Study of Acrylic and Methacrylic Fluorinated Polymer Coatings for Marble Protection.” *Prog. Org. Coat.*, **14** 47–57 (2018)
 48. Pan, H, Wang, G, Sun, Z, Ye, G, Sun, K, Pan, J, Zhang, J, Wang, J, “Surface Wettability Improvement of Heat Curing Acrylic Resin by Non-thermal Atmospheric Pressure Plasma.” *Acta Scientiarum Naturalium Universitatis Pekinensis*, **50** 235–241 (2014)
 49. Esmailpour, M, Niroumand, B, Monshi, A, Ramezanzadeh, B, Salahi, E, “The Role of Surface Energy Reducing Agent in the Formation of Self-Induced Nanoscale Surface Features and Wetting Behavior of Polyurethane Coatings.” *Prog. Org. Coat.*, **90** 317–323 (2016)
 50. Zhang, D-W, Wang, L-T, Qian, H-C, Li, X-G, “Superhydrophobic Surfaces for Corrosion Protection: A Review of Recent Progresses and Future Directions.” *J. Coat. Technol. Res.*, **13** 11–29 (2016)
 51. Feng, L, Zhu, Y, Wang, J, Shi, X, “One-Step Hydrothermal Process to Fabricate Superhydrophobic Surface on Magnesium Alloy with Enhanced Corrosion Resistance and Self-Cleaning Performance.” *Appl. Surf. Sci.*, **422** 566–573 (2017)
 52. Wenzel, R-N, “Resistance of Solid Surfaces to Wetting by Water.” *Ind. Eng. Chem.*, **28** 988–994 (1936)
 53. Amirudin, A, Thieny, D, “Application of Electrochemical Impedance Spectroscopy to Study the Degradation of Polymer-Coated Metals.” *Prog. Org. Coat.*, **26** 1–28 (1995)
 54. Zhang, Y, Shao, Y, Zhang, T, Meng, G, Wang, F, “The Effect of Epoxy Coating Containing Emeraldine Base and Hydrofluoric Acid Doped Polyaniline on the Corrosion Protection of AZ91D Magnesium Alloy.” *Corros. Sci.*, **53** 3747–3755 (2011)
 55. Yang, L-H, Liu, F-C, Han, E-H, “Effects of P/B on the Properties of Anticorrosive Coatings with Different Particle Size.” *Prog. Org. Coat.*, **53** (2) 91–98 (2005)
 56. Arukalam, I-O, Oguzie, E-E, Li, Y, “Fabrication of FDTs-Modified PDMS-ZnO Nanocomposite Hydrophobic Coating with Anti-fouling Capability for Corrosion Protection of Q235 Steel.” *J. Colloid Interface*, **484** 220–228 (2016)
 57. Zhang, J-T, Hu, J-M, Zhang, J-Q, Cao, C-N, “Studies of Water Transport Behavior and Impedance Models of Epoxy-

- Coated Metals in NaCl Solution by EIS.” *Prog. Org. Coat.*, **51** 145–151 (2004)
58. Njoku, DI, Cui, M, Xiao, H, Shang, B, Li, Y, “Understanding the Anticorrosive Protective Mechanisms of Modified Epoxy Coatings with Improved Barrier, Active and Self-Healing Functionalities: EIS and Spectroscopic Techniques.” *Sci. Rep.*, **7** 1–15 (2017)
 59. Hu, JM, Zhang, JQ, Cao, CN, “Determination of Water Uptake and Diffusion of Cl⁻ Ion in Epoxy Primer on Aluminum Alloys in NaCl Solution by Electrochemical Impedance Spectroscopy.” *Prog. Org. Coat.*, **46** 273–279 (2003)
 60. Sun, W, Wang, L, Yang, Z, Li, S, Wu, T, Liu, G, “Fabrication of Polydimethylsiloxane-Derived Superhydrophobic Surface on Aluminium via Chemical Vapour Deposition Technique for Corrosion Protection.” *Corros. Sci.*, **128** 176–185 (2017)
 61. Shi, A, Koka, S, Ullett, J, “Performance Evaluation on the Weathering Resistance of Two USAF Coating Systems (Standard 85285 Topcoat Versus Fluorinated APC Topcoat) via Electrochemical Impedance Spectroscopy.” *Prog. Org. Coat.*, **52** 196–209 (2005)
 62. Meng, F, Liu, L, Tian, W, Wu, H, Li, Y, Zhang, T, Wang, F, “The Influence of the Chemically Bonded Interface Between Fillers and Binder on the Failure Behaviour of an Epoxy Coating Under Marine Alternating Hydrostatic Pressure.” *Corros. Sci.*, **101** 139–154 (2015)
 63. Xu, L, Liu, F, Wang, Z, Ke, W, Han, E-H, Jie, G, et al., “The Effect of Surface Modification of Zinc Particles with Phosphoric Acid on the Corrosion Resistance of Cold Galvanizing Coatings.” *Prog. Org. Coat.*, **114** 90–101 (2018)
 64. Ding, R, Jiang, JM, Gui, TJ, “Study of Impedance Model and Water Transport Behavior of Modified Solvent-Free Epoxy Anticorrosion Coating by EIS.” *J. Coat. Technol. Res.*, **13** 501–515 (2016)
 65. Bose, S, Kuila, T, Uddin, ME, Kim, NH, Lau, AKT, Lee, JH, “In-situ Synthesis and Characterization of Electrically Conductive Polypyrrole/Graphene Nanocomposites.” *Polymer*, **51** 5921–5928 (2010)
 66. Canales, J, Muñoz, ME, Fernández, M, Santamaría, A, “Rheology, Electrical Conductivity and Crystallinity of a Polyurethane/Graphene Composite: Implications for Its Use as a Hot-Melt Adhesive.” *Compos. Part A Appl. Sci. Manuf.*, **84** 9–16 (2016)
 67. Tong, Y, Bohm, S, Song, M, “The Capability of Graphene on Improving the Electrical Conductivity and Anti-corrosion Properties of Polyurethane Coatings.” *Appl. Surf. Sci.*, **424** 72–81 (2017)
 68. Wang, Z, Han, E, Liu, F, Qian, Z, Zhu, L, “Waterborne Epoxy Nanocoatings Modified by Nanoemulsions and Nanoparticles.” *J. Mater. Sci. Technol.*, **30** 1036–1042 (2014)
 69. Li, Y, Gao, F, Xue, Z, Luan, Y, Yan, X, Guo, Z, et al., “Synergistic Effect of Different Graphene-CNT Heterostructures on Mechanical and Self-Healing Properties of Thermoplastic Polyurethane Composites.” *Mater. Des.*, **137** 438–445 (2018)
 70. Glikman, JF, Arnaud, R, Lemaire, J, Seinera, H, “Photolysis and Photooxidation of Ethylene Ethyl Acrylate Copolymers.” *Polym. Degrad. Stabil.*, **16** 325–335 (1986)
 71. Gerlock, JL, Smith, CA, Cooper, VA, Kaberline, SA, Prater, TJ, Carter, RO, Kucherov, AV, Msovski, T, Nochols, ME, “A Brief Review of Paint Weathering Research at Ford, Service Life Prediction.” *ACS Sym. Ser.*, **805** 212–249 (2001)

Publisher’s Note Springer Nature remains neutral with regard to jurisdictional claims in published maps and institutional affiliations.